

# Direct Spherical Calibration of Omnidirectional Far Infrared Camera System

David L Stone, *Member IEEE*, Guarav Shah, *Member IEEE*, Yuichi Motai, *Senior Member IEEE*

**Abstract**— We investigate the calibration of omnidirectional infrared (IR) camera for intelligent perception applications. Current omnidirectional camera approaches are primarily focused on omnidirectional color vision applications. The low resolution omnidirectional (O-D) IR image edge boundaries are not as sharp as with color vision cameras, and as a result, the standard calibration methods were harder to use and less accurate with the low definition of the omnidirectional IR camera. In order to more fully address omnidirectional IR camera calibration, we propose a new calibration grid center coordinates control point discovery methodology and a Direct Spherical Calibration (DSC) approach for a more robust and accurate method of calibration. DSC will address the limitations of the existing methods by using the spherical coordinates of the centroid of the calibration board to directly triangulate the location of the camera center and iteratively solve for the camera parameters. We compare DSC to three Baseline visual calibration methodologies and augment them with additional output of the spherical results for comparison. We also look at the optimum number of calibration boards using an evolutionary algorithm and Pareto optimization to find the best method and combination of accuracy, methodology and number of calibration boards. The benefits of DSC are more efficient calibration board geometry selection, and better accuracy than the three Baseline visual calibration methodologies.

**Index Terms**— Camera, Omnidirectional Camera Calibration, Far Infrared Camera, Direct Spherical Calibration, Visualization, Robot Sensing Systems.

## I. INTRODUCTION

While there has been a great deal of research in the area of camera calibration in general, and omnidirectional (O-D) camera calibration in particular, there has been little published work on the calibration of lower resolution O-D infrared (IR) cameras. The authors are leveraging the benefits of potentially low cost omnidirectional (O-D) infrared (IR) camera and color vision sensors applied to sensing for robot intelligent perception applications. The motivation for the calibration of the O-D camera is to lay the foundation for our work in vegetation detection, human tracking, and 3D scene reconstruction. The calibration helps us find the center of the camera and more accurately reconstruct the semantic geometry of the scene.

The existing omnidirectional camera calibration methods are optimized for visual cameras. The omnidirectional IR image edge boundaries are not as sharp as with color vision cameras, and as a result, the standard calibration methods were harder to use and in some cases

failed when applied to the low definition omnidirectional IR camera, and in some cases completely failed.

**Geometrical Approaches** - 3D omnidirectional geometry approaches are presented in [1-4]. The central catadioptric imaging process was shown in [5] to be a two-step projection process; first from the 3D world point  $X = (x, y, z)^T$  to a point on the unit sphere  $X_s = (x_s, y_s, z_s)^T$ , and from the sphere to a point  $m$  on the image plane  $m(u, v)$ .

**Survey of Methods** - [6] and [17] did surveys of methods. They surveyed about 25 methods, and was categorized into the four primary methods of omnidirectional calibration.

- **Direct Linear Transform (DLT) approach** - uses a spherical model and obtains a closed form solution using 3D - 2D correspondences.
- **Spherical-2D Pattern** - uses a spherical model coupled with multiple views of 2D pattern with as many points as possible in the pattern.
- **Distortion 2D Pattern** - Models the 2D images as distorted images and uses a Taylor expansion polynomial approximation as the projection function to find the distortion parameters.
- **Spherical Lines** - This approach uses the spherical camera model, a single omnidirectional image with at least three lines. The 3D lines are mapped to conics in the omnidirectional image.

The various methodologies are summarized in Table I below. Three of these methods (DLT-like, Spherical 2D Pattern, and Distortion-2D Pattern) showed good results with very similar performance. Of these three, the Distortion-2D Pattern approach had the best results in real world applications. All of these methods have been applied to omnidirectional color vision cameras but not to IR omnidirectional cameras.

The first two Baseline methods we used for comparison were chosen based on the best two methods found for visual omnidirectional camera calibration in the author's literature search. We also added a third more generic method for comparison. The three methods chosen to compare were Baseline 1: The Distortion-2D Pattern approach used by [7-8], and the Baseline 2: Spherical-2D Pattern approach [9]. The review of a radically different approach was also evaluated, Baseline 3: a generic calibration model [35, 36].

**Other methods** - were briefly evaluated and not used. A Direct Linear Transform (DLT) like approach is presented in [11]. The presentation of a hand-eye camera calibration approach which takes into account a lens distortion camera

TABLE I: METHODOLOGY SUMMARY

Method	Ref,	Model	Approach	Views
Geometry	[1-5]	N/A	Mixed	N/A
Survey	[6], [17]	N/A	Mixed	N/A
DLT	[11]	Sphere	Linear Eq.	Single
Distortion	[7-8],	Distort	Polynomi	Multi
2D	[12-13]		al	ple
Two-step	[10]	Planer	Joint	Single
Estimation		Motion	Optimizat	&
			ion	Odom
Overlappin	[14]	Lucas-	Bundle	Multi
g views		Kanade	adjust	ple
3D	[15]	Multiple	Mixed	Multi
Reconstruct		Observati		ple
Spherical	[9], [18]	Sphere	Single	Multi
2D			viewpoint	ple
Spherical	[3-5],	Sphere	Line	Single
Lines	[16],[19]		projection	
	[23-28]			
Straight	[20-22]	Lines	Vanishing	multi
lines, line	[31]	from	viewpoint,	ple
scan		motion,	line scan,	
		photogra	Multi-	
		mmetry	camera	
Visual	[22]	Camera	Bayesian	Movi
motion		Pose - two	Uncertain	ng
		spherical	y Analysis	camer
		images		a
Moving	[30]	N-view	SFM	multi
objects		matching		ple
Generic	[33, 34]	Planes	Multiple	Single
Multiple	[30]	2 mirror	IR point	Single
Spherical		optics	sources	
Surfaces				
Infrared	[35-37]	Not	Not	variou
		described	described	s
Non-	[38-39]	Optical	Multi axis	multi
standard		flow &	stereo	ple
		depth map		
Pareto	[40-41]	Pareto	Pareto	N/A
		Frontier	Optimize	

mode is given in [12-13]. The approach optimizes the intrinsic and extrinsic parameters using Kalman filter.

A 360 degree Distributed Aperture System composed of 6 narrow field of view cameras [14] is presented and uses forward additive Lucas-Kanade algorithm with bundle adjustment strategy to solve for offline estimation of camera orientation. A multiple observation 3D reconstruction is presented in [15]. A minimization of the re-projection error assuming that the angle of incidence between the point on the mirror is equal to the reflection angle or angle to the center of the mirror [16].

Calibrating the para-catadioptric camera from the projection of a sphere onto the image plane is also presented in [3-5], [16], [18-19], [23] and [28]. [20-22], and [31] applies line correspondences to generate re-projection error for calibration purposes. The authors use an offline calibration of surveillance cameras using camera height coupled with line geometries extracted from moving vehicles in the scene. In [31], the authors use the environment to find points, lines and planes in both the

image and the laser data to identify trihedron of lines from which to calibrate the camera and the laser.

The relationship of line and sphere invariant geometry and the projection of lines to conic curves are further investigated [23-28]. [30] Calibrates a multi-axial imaging systems consisting of a camera viewing multiple spherical reflecting or refracting surfaces to achieve wide angle views. Then from the rays of two or more spheres the pose of a single calibration grid is obtained by linear decomposition independent of the sphere locations and radius. The authors [33-34] give a generic calibration method that we used as our third baseline comparison.

Thermal point sources are presented in [35-36], but they do not present any calibration information. The authors in [37] use thermal cameras to measure odometry on a robotic platform. The calibration is accomplished using the standard checkerboard approach with the application of aluminum grid to improve the thermal reflectance. In [38-39] non-standard methods are used, an array of multiple micro lenses focused on the various scene light fields from the single primary lens to extract depth information from the different light fields from the scene, and multiple water droplets..

The contribution of this paper is the development of a new omnidirectional IR camera calibration framework, called Direct Spherical Calibration (DSC). Based on our experimental results, the DSC method fits in IR O-D sensing, because it provides IR O-D camera calibration with a more accurate and robust calibration board geometry selection, more direct calibration method, and better accuracy than the three Baseline visual calibration methodologies. Our approach can be generalized to other IR O-D cameras and should be applicable to visual cameras as well. The traditional approaches use a re-projection method based on unreliable control point resolution in the low resolution IR setting.

We propose a new omnidirectional IR camera calibration framework, called Direct Spherical Calibration (DSC). The contribution of this work follows:

- We apply a more robust corner selection method to overcome the problems with identifying the control points from the calibration grid in the lower resolution O-D IR camera. The process finds the key projection point more effectively for each calibration board with resultant improvement in calibration accuracy, when compared to the existing methods.
- We use a Direct Spherical Calibration method which results in higher accuracy when compared to traditional methods with sub-pixel accuracy.
- This work is original in that it more effectively calibrates the camera center and intrinsic and extrinsic parameters in order to more accurately reconstruct scene geometry.

The remainder of this paper is organized as follows: Section II describes the two Baseline omnidirectional camera calibration methodologies. Section III introduces the proposed omnidirectional geometry system approach, and the DSC methodology. Section IV provides the experimental setting and results for the omnidirectional IR camera calibration. Section V concludes the paper.

## II. DIRECT SPHERICAL CALIBRATION (DSC) OF OMNIDIRECTIONAL FAR INFRARED CAMERA

Section III proposes our new work Direct Spherical Calibration DSC, starting Section III.A, Omnidirectional IR camera geometry, Section III.B, Direct spherical omnidirectional IR camera calibration methodology, and Section III.C, Optimal number selection of image capture of calibration boards, and Section III.D Comparison to other methods.

### A. Omnidirectional IR camera geometry

The O-D camera operational setting is shown in Fig. 1 and is an example of an omnidirectional IR camera mounted on our Pioneer robot; the figure shows a) the camera on the robot, b) a sketch of the internal mirror, and c) a representative IR output. A car, a truck, and three people can be seen in the image. This paper is laying out the calibration approach and initial experimental results using data gathered with our camera mounted on the robot.

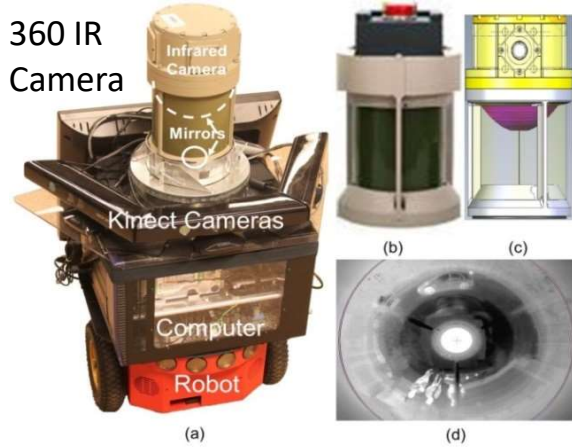


Fig. 1: Robot with Omnidirectional IR camera showing a) the Robot, b) the IR camera, c) the camera solid model showing the hemispherical mirror, and d) a representative output showing 3 people, a truck, and a car.

Using parabolic reflecting surfaces, a projected 360-degree field of view is created and transformed into a single 360 linear plane. With a single omnidirectional vision approach, Fig. 2, reconstructions of scenes create a reduced set of unknowns in the equations as compared to the many camera approach. The camera, parabolic mirror, and the geometry of the focusing lens and mirror are shown in Fig. 2, and is described in the equations (1-4) below:

$$r^2 = x_p^2 + y_p^2 \quad (1), \quad \theta = \tan^{-1}(y_p/x_p) \quad (2)$$

$$\varphi = \cos^{-1}(z/r) \quad (3), \quad z = (x_p^2 + y_p^2 - h^2)/2h \quad (4)$$

The IR camera is mounted in the housing above the parabolic lens, with a hole in the center of the lens. The

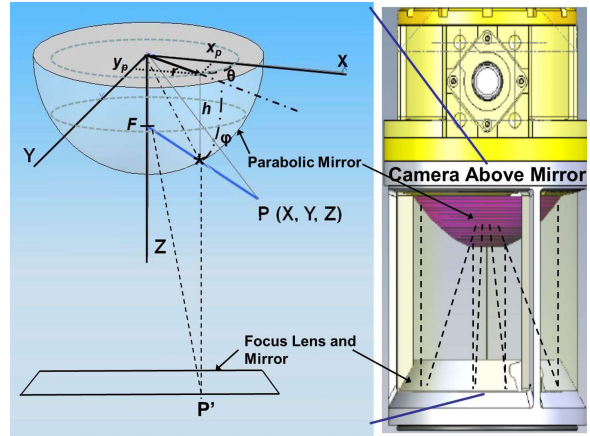


Fig. 2: shows the layout of the camera and the geometry of the omnidirectional parabolic mirror, and the relationship of the camera and focusing mirror/lens in the bottom of the structure. The Omnidirectional Camera geometry is presented, showing the relationship of the scene point P to the spherical point  $\rho$  and the  $x, y, z$  rectangular coordinates to the  $r, \theta, \varphi$  spherical coordinates.

point P in space is reflected from the parabolic mirror down to the base mirror P' and focused by the lower lens through the hole in the center of the parabolic mirror to the camera lens and image plane. F is the focus of the parabolic mirror. Where  $x_p$  and  $y_p$  are the pixel coordinates of the pixel, and P is the point in space being observed by the omnidirectional camera. In the spherical coordinate system  $\theta$  and  $\varphi$  define the direction of the ray and  $r$  is the distance to the origin of the mirror in pixel coordinates and  $\theta$  ranges from  $0^\circ$  to  $360^\circ$  around the edge of the mirror, and the pitch  $\varphi$ , ranges from  $0^\circ$  when pointing straight down, to  $90^\circ$  when pointing at the horizon. Fig. 3 shows the coordinate system in the O-D camera case, relating the  $(x, y, z)$  point to the sensor coordinate in  $(r, \theta, \varphi)$ . The camera geometry is shown in Fig. 2 Section IV. The  $(x, y)$  points in the world coordinates are related to  $(x_p, y_p)$  by equations (1-4). The orientation, Fig. 3 a) shows the omnidirectional IR sensor. The sensor annotated with the two coordinate systems is shown in Fig. 3b) with the  $r, \theta$ , and  $\varphi$  parameters overlaid. Fig. 3c) is the unwrapped image showing the relationship to  $x, y$ , and  $z$  coordinates,  $r$  is related to  $x, y$  by (1), and theta ( $\theta$ ) and Phi ( $\varphi$ ) to  $x, y$ , by (2) and (3),  $z$  is

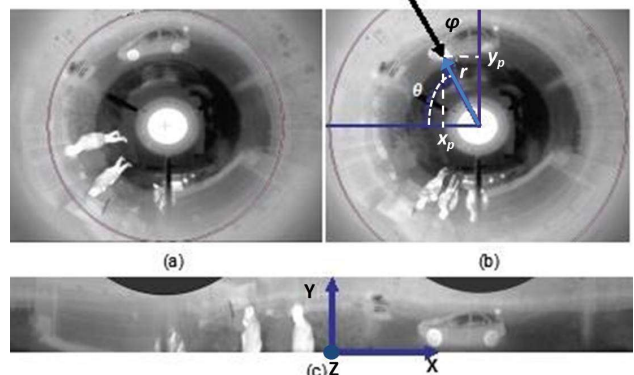


Fig 3: Omnidirectional geometry, (a) Shows the omnidirectional image, and (b) Shows the O-D IR image with the  $r, \theta$  geometry overlaid. (c) Shows the unwrapped rectangular image, and the X, Y, Z geometry axis.

related to  $r$  and  $h$  by (4).

*B. DSC omnidirectional IR camera calibration methodology*

With the IR image the edge boundaries are not as sharp as with color vision cameras. Fig. 4 shows an example of the calibration grid captured by the O-D IR camera, and the problem with accurately capturing the grid corner intersections in the low resolution calibration grid can be seen from the lack of clarity in some of the images sampled around the O-D IR camera. All of the baseline methods that we used for comparison used automatic corner selection which was not reliable in the lower resolution IR camera and required the authors to manually correct the baseline method's corner selection results. The poor quality of the grid selection in the lower resolution IR image resulted in higher error and in some cases a failure of the baseline calibration methods to converge. We propose a more effective calibration method using a direct triangulation approach.

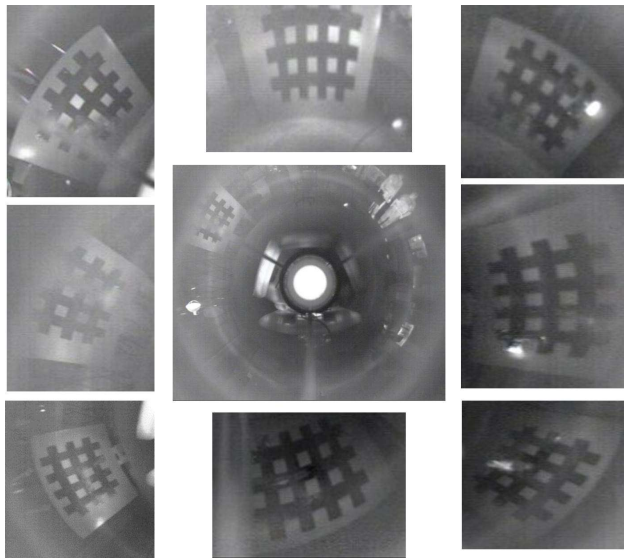


Fig. 4: Omnidirectional IR camera image and several representative calibration board grids. Due to the low resolution you can see the problem with accurately capturing the calibration control points.

As a result, the corner selection algorithms and automatic methods do not accurately find the corners. This affects both the error and the scatter in the error results. The newly proposed method, DSC, will address this by directly using the spherical coordinates of the centroid of the calibration board, found from the four outside corners of the calibration board grid, and will use the spherical coordinates of the calibration board center to directly calculate the re-projection parameters.

Fig. 5 shows a block diagram of the geometry transformation and the relationship of the spherical mirror to the captured calibration boards. The calibration process uses the planar calibration pattern to capture a matrix of spherical coordinates of the calibration board center points and then minimizes a least squares minimization function of the difference between the actual and re-projected points

to converge on the camera intrinsic and extrinsic calibration parameters.

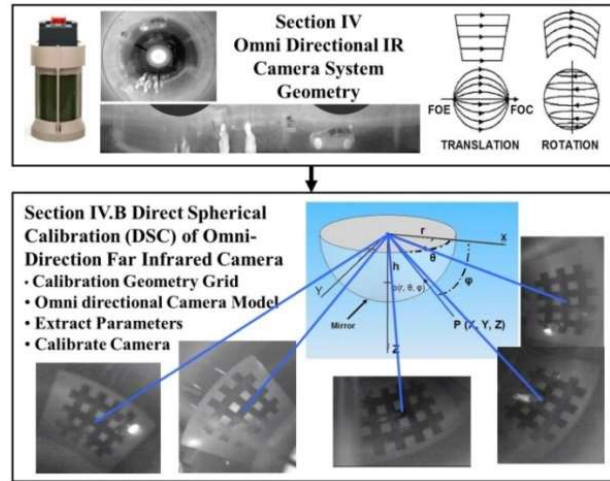


Fig. 5: Camera geometry and calibration: Capture the location of center of calibration boards at different radius and angle from the omnidirectional IR camera.

The proposed DSC consists of the six steps as follows.

**STEP 1: ESTABLISH A THERMAL CALIBRATION GRID 2D PLANAR PATTERN**

The calibration setup is shown in Fig. 6 and consisted of a pattern of reflective tape applied on a closely laid out grid with +/- 0.03215 accuracy on a white board with two IR heat lamps shining on the surface. The calibration board was calibrated by careful measurement of the grid spacing. Fig. 6a) shows the sensor on the robot with the board and heat lamps repositioned around the robot and camera. Three data sets were captured, sparse consisting of ten (10) images, moderate consisting of twenty-five (25) images, and dense consisting of forty-seven (47) images. The three setups were done on different days with the board and lamps being repositioned for each data image. The reflected image was then captured by the omnidirectional IR camera shown on top of the robot in Fig. 6a and 6b.

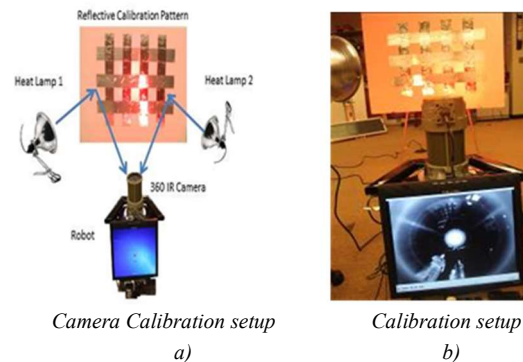


Fig. 6: Camera Calibration setup: a) Calibration setup diagram, with two heat lamps and a calibration board with thermally reflective pattern b) the calibration pattern illuminated by IR lamp with robot in foreground displaying Omnidirectional IR image.

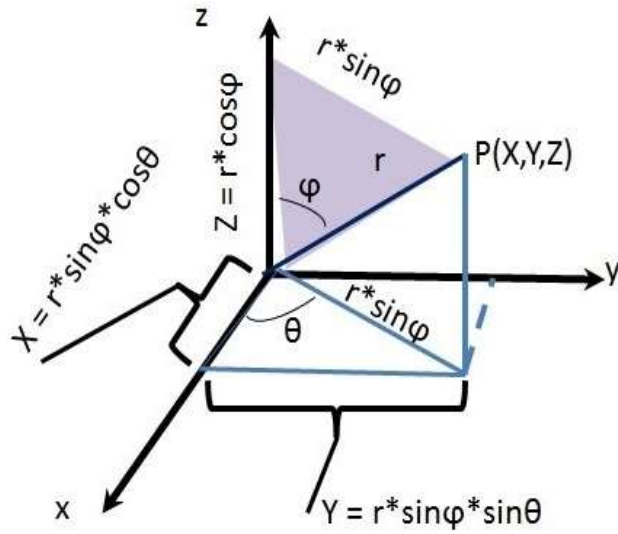


Fig. 7: Spherical Coordinate Diagram: Showing the relationship between Spherical Coordinates and Cartesian coordinates representing (8), (9), (10).

These images were then processed by the three algorithms for comparison. The method used in [31] to capture a calibration pattern from an LCD screen would not work with our IR O-D camera, due to the constant temperature of the screen. The methods used in [22 and 37] both used multiple cameras and were more complex than our setup. [22] Required a frame camera and a line scan camera, while [37] required an LCD projector, two stereo cameras and an IR camera. [30] used a single camera looking through multiple spherical lenses on different axis, this again was more complex than our setup and did not apply to our camera setup.

## STEP 2: DIRECT SPHERICAL CALIBRATION (DSC) CAMERA MODEL

The DSC methodology uses the direct spherical coordinates of the calibration grids in equation (11) below to find the projection error. The process then minimizes the error in order to solve for the intrinsic parameters (5).

The world point  $P(X, Y, Z) = (x, y, z)^T$  is projected to a point on the unit sphere  $X_s = (x_s, y_s, z_s)^T$ , and from the sphere to a point  $m$  on the image plane  $m(u, v)$ .  $K_c$  equation (5) is the intrinsic camera parameter matrix.

$$K_c = \begin{bmatrix} \gamma_x & s & u_0 \\ 0 & \gamma_y & v_0 \\ 0 & 0 & 1 \end{bmatrix} \quad (5)$$

Where focal length is  $\gamma_x, \gamma_y$ ,  $s$  is the image skew, and  $p(u_0, v_0, 1)^T$  the principal point. The skew  $s$  is affected by both the focal length ( $\gamma$ ) and the aspect ratio  $\alpha$ . The imaging projection process is then captured by extending the single view point camera model  $m = K_c [R \ t] X$  relating the space point matrix  $X$ , intrinsic parameters  $K_c$ , the extrinsic parameters  $R'$  and  $t$  to the image projection matrix  $m(u', v')$  and are substituted in equation (6).

$$\beta m = K_c \left( \frac{R'X + t}{\|R'X + t\|} \right) + \xi e \quad (6)$$

where  $\beta$  is a scale factor,  $R'$  is a 3 x 3 rotation matrix,  $t$  is

the vector of translation  $t = (t_x, t_y, t_z)^T$  and  $\xi$  is the mirror shape parameter. The mirror is a paraboloid if  $\xi = 1$ , an ellipsoid or hyperboloid if  $0 < \xi < 1$ , and a plane if  $\xi = 0$ .  $R'$  is the mirror to camera rotation matrix, and  $t$  is the mirror to camera translation matrix as before.

The eccentricity  $e$  is a vector of the eccentricity in the  $x$ , and  $y$  direction and is a measure of how much the cross section deviates from being circular. The values and their interpretation are given below.

The eccentricity of a circle is zero.

- The eccentricity of an ellipse which is not a circle is greater than zero but less than 1.

- The eccentricity of a parabola is 1.

- The eccentricity of a hyperbola greater than 1.

The relationship between  $\xi$  and  $e$  is given in equation (7) and summarized in Table II.

$$\xi = \frac{2 * e}{1 + e^2} \quad (7)$$

Both  $\xi$  and eccentricity ( $e$ ) were iterated during the calibration.  $\xi$  converged towards 1.0 and  $e_x, e_y$  converged towards 1.0. In our case the IR omnidirectional camera with parabolic mirror, the relationship between the world point  $(X, Y, Z)$  and the spherical point  $(r, \theta, \phi)$  are given by applying trigonometry as in Fig. 7 and as noted in equations (1) to (4), and resulting in equations (8), (9), and (10).

$$X = r \sin \phi \cos \theta \quad (8)$$

$$Y = r \sin \phi \sin \theta \quad (9)$$

$$Z = r \cos \phi \quad (10)$$

The world point vector  $X$  (6) is replaced by its spherical coordinate equivalent elements from equations (8), (9), and (10) resulting in (11). The initial  $(r, \theta, \phi)$  points are substituted into (11) along with the estimated  $K_c, R'$ , and  $t$

TABLE II: RELATIONSHIP BETWEEN ECCENTRICITY  $e$  AND MIRROR PARAMETER  $\xi$

	Ellipsoidal	Paraboloid	Hyperbolical	Planar
$e$	$0 < e < 1$	$e = 1$	$e > 1$	$e \rightarrow \infty$
$\xi$	$0 < \xi < 1$	$\xi = 1$	$0 < \xi < 1$	$\xi = 0$

matrices and the projection point is calculated, the cost function  $f(x)$  is then minimized.

$$\beta m = K_c \left( \frac{R' \begin{bmatrix} r \sin \phi \cos \theta \\ r \sin \phi \sin \theta \\ r \cos \phi \end{bmatrix} + t}{\left\| R' \begin{bmatrix} r \sin \phi \cos \theta \\ r \sin \phi \sin \theta \\ r \cos \phi \end{bmatrix} + t \right\|} \right) \quad (11)$$

$f(x) = \frac{1}{2} \sum_1^n [P(x_i) - e_i]^2$ , where  $n$  is the number calibration boards,  $P(x_i)$  is the projected calibration board center, and  $e_i$  is the extracted calibration board center. The cost function is the Euclidian distance between the projected calibration board center point and the extracted value in the image. The  $n$  calibration board re-projection points are then used to triangulate the camera center. Equation (11) represents the calibration equation directly in the  $(r, \theta, \phi)$  framework, and is used to find the re-projected calibration points, and the fitness function  $f(x)$  is then minimized using Levenberg-Marquardt approach. It is the relationship between the intrinsic, extrinsic

parameters and the camera geometry.

### STEP 3: MEASURE THE GRID CORNER (4 OUTSIDE) INTERSECTION POINTS

Our method of selecting the four outside corners as a starting point and applying our algorithm to find the position of the calibration board center worked significantly, on the order of 40X, better than the baseline methods. The baseline methods saw errors on the order of 81 pixels compared to ours at 2 pixels. The baseline methods struggled with the low resolution IR images which either introduced larger error, or failed completely to converge. The calculated coordinates of the center of the calibration board was then used to directly calculate the spherical coordinates and the projected radius to the center of the camera was found by minimizing the re-projection error.

The four corners of each calibration grid in the data set images, Fig. 8, are clicked on by the user with a corner assist algorithm, with an accuracy of +/- 2 pixels, and the pixel coordinates of the corners are extracted and the central point of the grid (green square at the center of the distorted corners box) is approximated by geometry of the four image points.

We first attempted the MATLAB automatic corner selection [32] used in [31], but this method broke down on our lower quality IR images necessitating our modified approach. The internal extrapolation failed and the internal points being out of position resulted in the error solution going out of bounds in some of the images. This necessitated us to estimate the center from the geometry of the four outside corners which worked much better. The image coordinates of the entire calibration board center points are then used to find the  $\theta$ ,  $\phi$  and  $r$  value of the calibration board centers which are then substituted into (11) and the difference between the projected points and the observed image points are minimized.  $\theta$ , and  $\phi$  are the angles to the center of the capture board grid observed from image coordinates, and  $r$  is the distance from the center of the camera to the center of the capture board in pixel coordinates obtained from equations (1-4). The value of  $r$  is found by  $r = \text{sqrt}(x_p^2 + y_p^2)$ , and  $x_p$  and  $y_p$  are the pixel coordinates of the grid center in the image. The  $\theta$ ,  $\phi$  and  $r$  values are substituted into (11) from step 2.

### STEP 4: SOLVE FOR THE CAMERA INTRINSIC PARAMETERS (Kc)

The  $K_c$  matrix (5) is then solved for and the results displayed. The  $(r_c, \theta_c)$  is re-projected on the image and the error is minimized to find the solution to (11). This DSC direct approach has the best calibration results when compared to the Baseline1 (distortion) and 2 (single viewpoint spherical) methods, but with smaller error. Baseline 3 (generic) had much higher error and went out of bounds on the dense data set.

### STEP 5: SOLVE FOR THE CAMERA EXTRINSIC PARAMETERS

The calibration process then finds the  $R'$  and  $t$  matrices

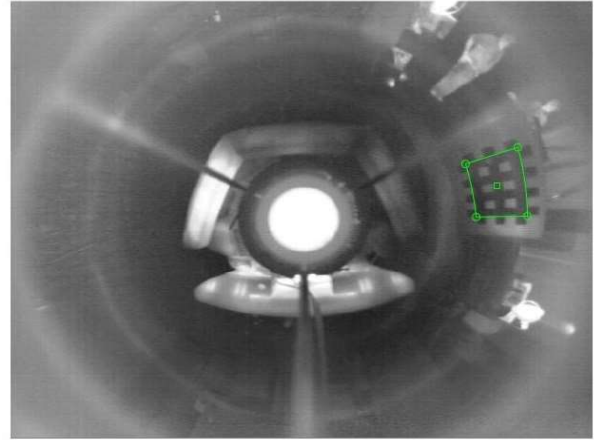


Fig. 8: Calibration Board center approximation.

such that a least square error function is minimized to best match the mapping, and the process iterated until convergence or threshold is met.

### STEP 6: ITERATE STEPS FOUR AND FIVE UNTIL CONVERGENCE.

Since the intrinsic and extrinsic parameters are related we iterate steps four and five until the minimized re-projection errors converge. The six steps are summarized in Table III. The results of our DSC method and the three Baseline methods will be presented in Section IV.B.

TABLE III: FIVE PROCESS STEPS FOR DSC

Steps	Step Details
Step 1	Establish a thermal calibration grid 2D Planer Pattern with thermally reflective grid of known geometry, which consisted of five rows of seven squares or a total of 48 corner points. (needed for Baseline methods) The grid was constructed on a white board with a cross pattern of silver reflective tape. The calibration boards were then used at different angles and distances from the camera. (DSC only used the outside corners)
Step 2	Direct Spherical Calibration (DSC) Establish the DSC Camera Model in terms of $(r, \theta, \phi)$
	$\beta m = K_c \left\{ \begin{array}{l} \frac{r' \sin \phi \cos \theta}{r \cos \phi} + t \\ \frac{r' \sin \phi \sin \theta}{r \cos \phi} + t \\ \frac{r' \sin \phi \cos \theta}{r \cos \phi} + t \end{array} \right\} + \xi e$
Step 3	Measure the grid corner (4 outside) intersection points at different unknown positions which are related to the sensor coordinate system by a rotation matrix $R' = [R'_x, R'_y, R'_z]$ and translation matrix $t = [t_x, t_y, t_z]$ , the extrinsic parameters
Step 4	Solve for the camera intrinsic parameters $K_c$
	$K_c = \begin{bmatrix} \gamma_x & s & u_0 \\ 0 & \gamma_y & v_0 \\ 0 & 0 & 1 \end{bmatrix}$ Where $s$ is the skew and is a function of $\alpha$ the camera aspect ratio and the focal length, $\gamma$ is the focal length, and $u_0, v_0$ is the principal point.
Step 5	Solve for the camera extrinsic parameters $R' = (R'_x, R'_y, R'_z)^T$ , $R'$ is the camera rotation about the $x, y, z$ axis. $t = (t_x, t_y, t_z)^T$ , $t$ is the translation of the camera along the three $x, y, z$ axis.
Step 6	Iterate steps 2 - 5 until convergence since the intrinsic and extrinsic parameters influence each other.

### C. Optimal number selection of image capture of calibration boards

Pareto optimization is a methodology commonly used for multi-variant optimization problems. Visualization techniques are described for multi-dimensional optimization problems using multivariate mesh displays, color mappings, and multiple views [40]. Techniques for multi-variant objective optimization are given in [41].

We will use Pareto optimization as an analysis tool to find the optimum calibration approach and number of calibration board images. This section determines the effect of the number of calibration board images on the calibration results. The methodology used to find the optimum number of calibration capture boards is to find the optimal calibration condition when minimizing the error during the determination of the intrinsic camera matrix  $K_c$  (5), and also minimizing re-projection error. To accomplish this optimization, we will use a MATLAB Pareto optimization to find the min. function that best satisfies error, ratio of calibrated to actual and time minimization.

Fig. 9 describes the Pareto optimization concept which is for the minimization of multiple objective factors. In an optimization problem it is typically the evaluation of decision variables by minimizing a cost function. However, in most real life optimization problems the cost function is multi-dimensional trying to satisfy multiple objectives. This is our case, the example shown in Fig. 9, the two cost objectives are re-projection error  $\epsilon_d$  and time  $t$ .

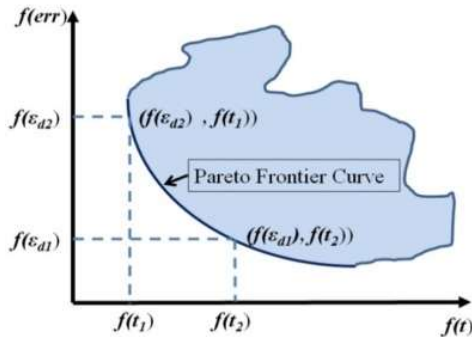


Fig. 9: Pareto Optimization Diagram: Showing an example Multi-objective optimization space and the Pareto frontier curve representing the loci of points satisfying both objectives ( $\epsilon_{d_i}$ ,  $t$ ) optimal number selection of image capture of calibration boards

The Pareto Frontier curve shown represents the set of solutions that satisfy the minimization of both constraints according to the fitness function  $f$ . In the Fig. 9 example  $f(\epsilon_{d1}, t_2)$  as well as  $f(\epsilon_{d2}, t_1)$  are both optimum solutions, and lie on the pareto optimized frontier. We will use a three objective fitness function to simplify the Pareto optimum frontier, where the three objectives are the ratio of calibrated to actual ( $R_{CA}$ ) of distance and angle distribution in the polar coordinate, re-projection error ( $\epsilon_d$ ), as obtained from the calibration process, and process time ( $t$ ). While time ( $t$ ) is not important from an operational viewpoint since the calibration is done off-line, it was chosen as a

comparison parameter between the three methods.

The Pareto optimization would find all points ( $R_{CA}$ ,  $\epsilon_d$ ,  $t$ ) in the objective space that satisfy our scalar fitness function, equation (12).

$$Arg_{n_{min}} = f(R_{CA}, \epsilon_d, t) = \sqrt{(|R_{CA} - 1|^2 + \epsilon_d^2 + t^2)} \quad (12)$$

We used the MATLAB Pareto Optimization Tool Box to find the global optimum for the four methods and data sets. Ratio of Calibrated to Actual data is given as  $R_{CA}$ . An example of the concept is shown in Fig. 10 with perfect desired  $R_{CA}$  given as the blue circle with  $R_{CA} = 1.0$ . The red curve represents the actual  $R_{CA}$  and varies around the perfect ratio of  $R_{CA} = 1.0$ . The  $R_{CA}$  is given by equation (13),

$$R_{CA} = \frac{(R_R + R_A)}{2} \quad (13)$$

Equation (13) is used as a common shape factor.

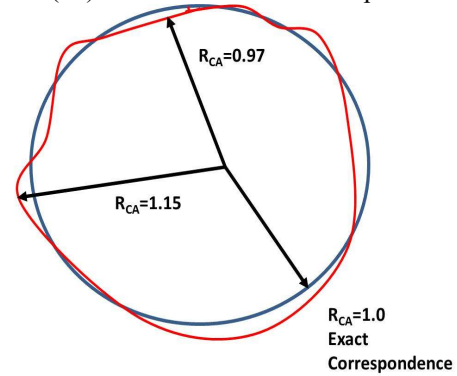


Fig. 10. Ratio of calibrated to measured data as a shape factor, where  $R_{CA} = 1.0$  is perfect correspondence and is represented by the blue circle. The red curve is the actual variation  $R_{CA}$  about the blue circle.

Where  $R_R$  is the ratio of calibrated to measured radius and  $R_A$  is the ratio of calibrated to measured angle.

The evaluation criteria for  $R_{CA}$  will be the absolute value of the difference between the ratio of calibrated to measured ( $R_{CA}$ ) and the perfect correspondence of 1.0 as  $|(R_{CA} - 1)|$ . The error parameter is the mean of the re-projection error as a function of the diameter of the plotted re-projection circle.  $\epsilon_d$  is given by equation (14) as a re-projection error.

$$\epsilon_d = \text{mean} \left( \left| \text{sqrt}(d_{actual} - d_{re-projected})^2 \right| \right) \quad (14)$$

The last parameter time ( $t$ ) is the period during the calculation of the calibration modules proposed in Section IV.B and is given by  $t = (\text{time at finish} - \text{time at start})$ . The relationship between the Ratio of Calibrated to Actual ( $R_{CA}$ ), error ( $\epsilon_d$ ), and time ( $t$ ) will be explored in the experimental results section.

### D. Comparison to other methods - Baselines 1,2,3

In this paper our method plus three existing methods for identifying checkerboards on calibration images were analyzed. The four methods are compared in Table IV. From the three, two Baseline methods were chosen as the best candidates to modify for the O-D IR camera calibration, and the best methods of both were combined

TABLE IV: METHODOLOGY COMPARISON

Criteria	Baseline 1 distortion [7-8]	Baseline 2 single viewpoint spherical [13]	Baseline 3 generic [36-37]	DSC
Model	Distortion	Spherical	Distortion	Spherical
Points Re-projected	25 x 48	25 x 48	25 x 20	25 x 1 (centroid)
Mirror	Spherical	Spherical	Spherical	Spherical
Approach	Poly-nominal Approx.	Single Viewpoint	Generic	Direct Spherical

with our methodology for an improved method for calibrating IR omnidirectional cameras. An exhaustive comparison of other methods was not the purpose of this work. The methods chosen then served as the starting point for the adapted and improved DSC method described in Section IV. Due to the quality of thermal images the edge boundaries were not as crisp as visual images. As a result, the automatic corner finders had marginal performance. Often all three comparison methods would provide poor results when the corners were poorly selected even in the manual mode with corner assist. This required extensive manual tuning in the Baseline 1 (distortion) [7-8], and 3 (generic) methods. The Baseline 2 (single viewpoint spherical) method used the four outside corners as a starting point but still calculated the internal grid points which took more time and was prone to error with the IR images if the points weren't well chosen. In the dense data set case all three baseline methods had trouble with the partially obscured calibration boards due to the camera structure. This caused an extensive amount of rework making these methods not practical for the lower quality IR images.

The DSC direct spherical method used the four outside corners of the calibration grid to find the calibration board center point and this pixel spherical coordinate was then used to directly calibrate using the one spherical point for each calibration board. The geometric center of the whole grid is then calculated from these four geometric points and the spherical coordinates of the center of the grid is used in the calibration. This avoids the errors introduced by finding a best fit of the line matching of the individual grid square elements (which does not work well in the IR case) to establish the calibration geometry. Our results show that this improves the calibration accuracy, and requires less data entry time. The method also has the best computational performance.

### III. EXPERIMENTAL RESULTS

Section IV.A describes the data setting for the evaluation. Section IV.B applies the DSC methodology presented in Section III, Section IV.C compares DSC to the three Baseline methodologies, Section IV.D presents the error analysis of four methods, and IV.E presents the results of the optimum number for capture of calibration boards.

#### A. Calibration data setting for evaluation

In the use of the omnidirectional IR camera, a camera calibration process is required just as in a conventional vision system. The three calibration data sets were taken in separate setups. The sparse set had fair quality, some partial obscuration from the support bars on the camera, and moderate clarity. The moderate data sets had good quality and good clarity.

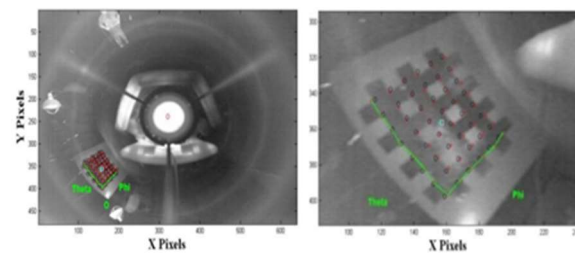
Table V describes the characteristics of the three data sets used for the evaluation. The resulting images were visually inspected to determine if the quality and clarity of the images were sufficient for the calibration work. The images were also evaluated to determine if the vertical support bars of the camera significantly obscured the view of the calibration boards.

TABLE V: TEST IMAGE SETS

Image set	# Image	Resolution	Obscured	Clarity
Sparse Set	10	61%	Four partial	4 of 10 clear
Moderate Set	25	70.4%	Five Partial	16 of 25 clear
Dense Set	47	53%	Fourteen Partial	28 of 47 clear

The dense data set had marginal quality. The moderate set had no images obscured while the dense had the most partial obscuration with ten out of forty-seven of the calibration board views. These rankings were subjectively determined by visual observation of the images.

Fig. 11 shows a sample of calibration points picked by the operator using the Baseline 1 (distortion); Scaramuzza *et al.* methodology, and a typical re-projection of the calibration points onto the original pattern.



a) Re-projection on grid      b) Zoomed in calibration grid

Fig. 11: Example of re-projection points in the Baseline 1 (distortion) method with a) Grid points chosen for calibration and re-projection of points onto the calibration pattern. b) Zoomed in view of the calibration grid.

We modified the plot to show the theta and phi directions on the plot. The heat lamps can be seen in the images as well as the reflected calibration grids. Utilizing the four methods; our DSC method, the Baseline 1 (distortion) method [10 - 12], the Baseline 2 (single viewpoint spherical) method [13], and the Baseline 3 (generic) method [41-42]; each calibration methodology was applied to the IR catadioptric camera using a calibration pattern of a white board with thermal reflective tape making a grid pattern that could be used to create a

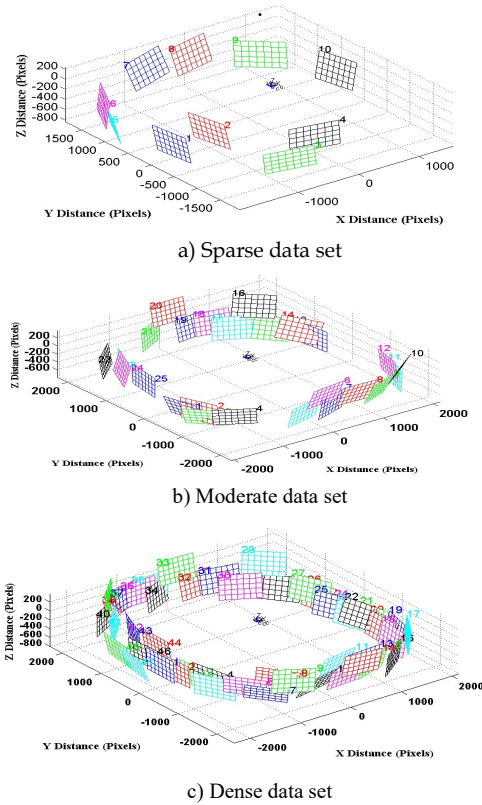


Fig. 12: Extrinsic mapping of the three data sets, a) sparse data set with 10 calibration images, b) moderate data set with 25 calibration images, c) dense data set with 47 calibration Images,

thermally reflective pattern on the board. The checkerboard pattern was required by the three Baseline methods. As a result, the DSC method used the same checkerboard pattern that was used for the three Baseline methods for a more direct comparison. Even though our method only used the outside corners to find the center, we wanted to be able to compare to the results for the other methods directly without introducing additional factors. The images were then captured and the four methodologies applied. The experimental result comparisons are presented in Section IV.B and IV.C. Fig. 12 is the data setting and shows the extrinsic projection of the three data set positions around the camera.

### B. DSC calibration

Our DSC approach was adapted to more effectively work with an omnidirectional IR camera, and to improve the accuracy over the Baseline methods. The DSC methodology approach to the corner selection dramatically reduced the error introduced by the Baseline corner and blob selection approaches due to their algorithm failing when given the low resolution of the IR image, and Fig. 13 presents the comparison of the DSC to the baseline methods for the sparse (10 calibration images) data set.

The plots in Fig. 13 represent the average error of the four methodologies across the calibration boards. The error for the DSC method was the smallest and was on the order of  $0.2$  to  $0.5 \times 10^{-4}$  pixels for all of the sparse data

set. Baseline 2 (single viewpoint spherical) was next best with 1-2 pixel error, Baseline 1 (distortion) with 2-3 pixel error, and finally Baseline 3 (generic) with error on the order of 8-19 pixels of error.

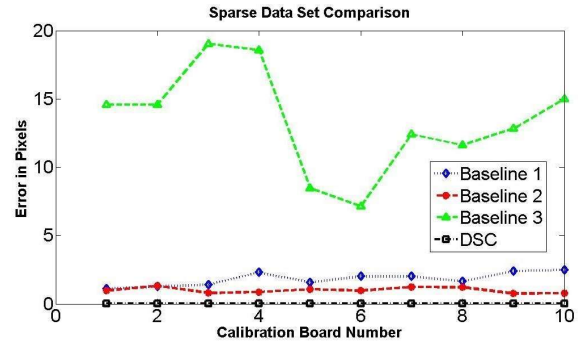


Fig. 13: Comparisons of the re-projection error for the three Baseline methods with our DSC method. The results are shown for the sparse data set case. The DSC method has the lowest error followed by Baseline 2 (spherical), then Baseline 1 (distortion) and finally Baseline 3 (generic) as the worst.

Note that Baseline 1 (distortion) and 3 (generic) both tended to go out of bounds due to poor geometry selection with the lower quality IR images and required an inordinate amount of hand adjustment to get them to work. Fig. 14 shows the comparison of the four methods for the moderate data set blurred IR images. The calibration images were captured and processed using our DSC methodology. The corner selection methodology was an initial manual selection with corner assist to find the entire capture board grid and then find the center of the grid. We used the direct spherical coordinates of this calculated center point for each calibration board grid as the input to the DSC calibration. This worked much better for the IR images and significantly cut down the analysis time. This method was more robust to the poor edge quality of the IR image.

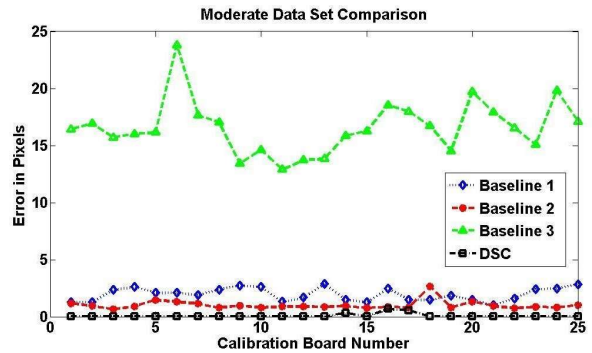


Fig. 14: Comparisons of the re-projection error for the three Baseline methods with our DSC method. The results are shown for the moderate data set case. The DSC method has the lowest error followed by Baseline 2 (single viewpoint spherical), then Baseline 1 (distortion) and finally Baseline 3 (generic) as the worst.

### C. Comparison to other Baseline calibration methods

Among the existing color vision omnidirectional camera calibration methodologies, we chose the two best performing methods plus one more generic method for

comparison.

The Baseline 1 (distortion) omnidirectional camera calibration methodology, [7], [8], [9] proposed a polynomial approximation distortion model with 2D patterns approach.

In the Baseline 2 (single viewpoint spherical) methodology [10], single view point re-projection method uses a distortion model of the camera properties with a single viewpoint spherical projection model where the world points are projected onto the unit sphere. They then use a secondary projection onto a normalized plane.

In the Baseline 3 (generic) methodology [34-35] was chosen as a more generic method intended for a wide range of camera types. It uses a generic model of the camera properties that could handle different types of cameras including conventional perspective, central omnidirectional (including catadioptric, fish-eye, and generic central lens), and finally non-central cameras. The approach utilizes two Fourier series polynomial distortion terms in the calibration process. The distortion model is more generic and not based on the perspective projection.

The three Baseline calibration methodologies were compared to our DSC methodology. As the data for the DSC shows the smallest error with the moderate data set having 22 out of 25 calibration boards with error less than  $1 \times 10^{-4}$  pixels with a couple of sub-pixel error outliers. The DSC moderate data set has three outliers at 0.34, 0.54, and 0.69 pixels.

Again the Baseline method 1 and 3 methods required many tries at getting the solution not to go out of bounds and this was very labor intensive since the automatic corner finding routine was optimized for visual omnidirectional images and wouldn't work with the lower quality IR images, this made the method 1(distortion) and 3 (generic) methods automatic selection of points unreliable. Additionally, the manual corner selection was error prone causing the routine to blow up and fail necessitating rework. This was quite time consuming and took about a week of 5-6 hours a day making manual corrections to the corner coordinates for Baseline 1 (distortion) and similar timeframe with Baseline 3 (generic) trying to get the solution to work. This still did

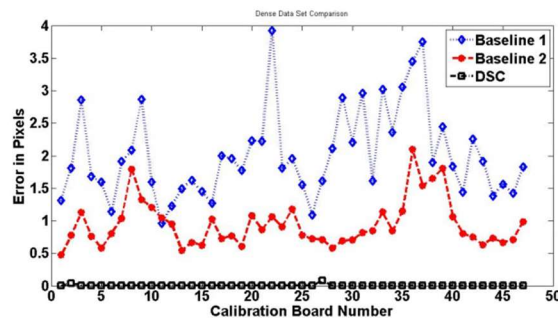


Fig. 15: Comparisons of the re-projection error for the three Baseline methods with our DSC method. The results are shown for the dense data set case. The DSC method has the lowest error followed by Baseline 2 (spherical), then Baseline 1 (distortion) and finally Baseline 3 (generic) as the worst.

not correctly find all the corners. This required us to go into the images and manually reposition about a third of the corners on about half of the images. After this correction the max and average errors behaved much better. Fig. 15 shows that the error comparison for the moderate data set was similar to the sparse case with DSC best, Baseline 2 (single viewpoint spherical) next, Baseline 1 (distortion) next with 2-3 pixel error, and finally Baseline 3 (generic) with 13-25 pixel error.

Fig. 15 shows the comparison of the methods for the dense data set. We were not able to show the Baseline 3 (generic) since after a week of attempting to get it working the program would crash when trying to find the calibration points in the low quality IR image.

As before with the sparse and moderate data sets DSC is the best with sub pixel error with only two outliers near 0.1 pixel and the rest less than  $10^{-5}$ . Baseline 2 (single viewpoint spherical) is next with 1-2 pixel error, and Baseline 1 (distortion) with 1-4 pixel error. Again Baseline 3 (generic) would blow up.

*D. Error analysis of four methods*

In Fig. 16 we compare the x, y error scatter for the four methodologies. a) DSC error as a function of x, y scatter, the DSC is displayed at a different scale so the scatter can be seen. b) Baseline 1 (distortion) error as a function of x, y scatter, c) Baseline 2 (spherical) error as a function of x, y scatter d) Baseline 3 (generic) error as a function of x, y scatter. It can be seen that the least error scatter is for the DSC method, the worst for Baseline 3 method then Baseline 1 and finally Baseline 2. Unlike the other methods, the DSC has one error point per calibration board, where the others have points for the total number of intersections in the calibration boards.

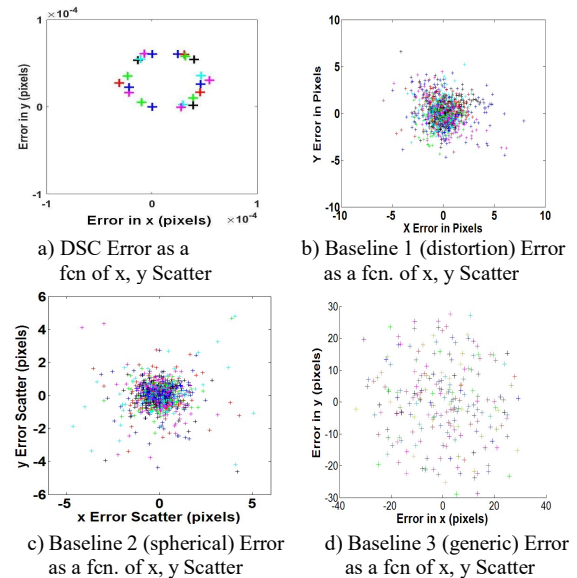


Fig. 16: Comparison of the error as a function of x, y scatter for the four methods. Only the moderate data set is shown. a) DSC method (different scale to show scatter), b) Baseline 1 (distortion) Method, c) Baseline 2 (single viewpoint spherical) method, d) Baseline 3 (generic) method.

Fig. 17 shows the error data as a function of radius for the four methodologies. The blue curve in Fig. 17 represents the median of the scatter data for each method. Fig. 17a) DSC error as a function of radius, the DSC is displayed at a different scale so the scatter can be seen. 17b) Baseline 1 (distortion) error as a function of radius, 17c) Baseline 2 (single viewpoint spherical) error as a function of radius 17d) Baseline 3 (generic) error as a function of radius. The blue curve in Fig. 17a) represents the median of the error data and is near zero for the DSC methodology. Again the DSC method has one point per calibration board. It can be seen that the DSC has a similar but smaller spread in angle, but an order of magnitude smaller spread in radius error.

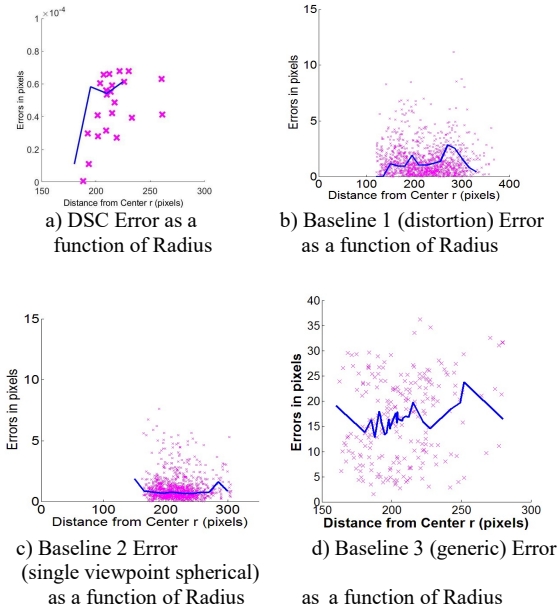


Fig. 17: Comparison of the error as a function of radius for the four methods. Only the moderate data set is shown. a) DSC method (different scale to show scatter), b) Baseline 1 (distortion) Method, c) Baseline 2 (spherical) method, d) Baseline 3 (generic) method The mean of the error scatter is overlaid as the blue curve.

The average error for Baseline 1 (distortion) is 2 pixels where the max scatter is up to 10 pixels, and Baseline 2 (single viewpoint spherical) average error is 0.94 pixels and the max error is about 7 pixels. The DSC error is sub pixel and on the order of a thousandth of a pixel. The DSC, Baseline 1 (distortion), and Baseline 2 (single viewpoint spherical) methods track fairly close in finding the center.

Baseline 1 and 2 methods found the center within 4 pixels, and the DSC was within 1 pixel. With the Baseline 3 (generic) method, the center is off by 68.8 pixels in the y direction. The actual center is about 324, 241 which is matched closest by the DSC method at 323.75, 240.86. There is a 5% delta in focal length. The uncertainty associated with the average errors is lowest for DSC at 0.00192 followed by BL2 at 0.05819, BL1 at 0.1011, and finally BL3 at 0.4707.

The DSC methodology is better than the other three Baseline methods with smaller error and less uncertainty, as shown in Table VI.

TABLE VI: METHODOLOGY NUMERICAL COMPARISON

Framework	DSC	BL1 distortion	BL 2 single viewpoint spherical	BL3 generic
Average Error	0.00265	2.0057	0.94	16.5660
Standard Deviation	0.013	0.6928	0.3557	13.9032
Uncertainty	0.00192	0.1011	0.05819	0.4707
Calibration Time	0.017	2.09	53.43	325.2127
Center	323.75, 240.86	321.02, 239.96	323.50, 244.34	322.7239, 309.8056
Focal Length	264.99, 264.99	N/A, N/A	251.01, 253.75	313.0189, 253.9237

We have included in Table VI a fourth column showing the Baseline 3 methodology [35,36] that had much higher errors compared to the other two Baseline methods and it didn't work well with the IR data. Also, it can be seen in Fig. 16 that the Generic method's error is on the order of 30 pixels and is much higher than the other two Baseline methods chosen for comparison. Also, Baseline 3 (Generic) missed the center by 68.8 pixels. It can be seen from Table VI that the DSC method is the best performer.

#### E. Optimal number selection of image capture of calibration boards

We did an analysis to determine the optimum number of calibration boards. We compared Ratio of Calibrated to Actual, error, and computation time. Fig. 18 is our plot of the three methodologies in polar form showing the relative comparison of the  $r$ ,  $\theta$  polar points obtained from the three methodologies.  $\phi$  was nominally 90 degrees and relatively constant for all methods so it was not presented. Fig 18 shows the  $R_{CA}$  in a comparison polar line plot for

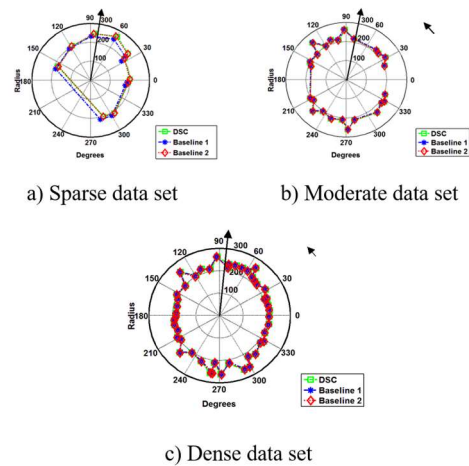


Fig. 18: Comparison polar plot of the  $r$ ,  $\theta$  for DSC compared to the two Baseline methodologies. For a) sparse data 10, b) moderate data 25, and c) dense data 47 calibration board images. The main three data sets  $r$ ,  $\theta$  compare reasonably well with the ground truth with the delta being roughly 5% for all three.

the moderate data set. The moderate case has the best match to the actual data for the four methods. The three Baseline methods did not originally present this data, but we added it to all of their routines for comparison. The polar plot shows the comparison of the best three methodologies in finding the  $r, \theta$  (theta) points for each of the data sets. The baseline 3 (generic) method had an average 19% error (peak 64%) in  $r, \theta$  compared to ground truth measurements, so it wasn't included in the polar plot. The sparse data set with only ten (10) calibration boards had the least consistency between the three methods. For the DSC and Baseline 1 and 2, all three matched the ground truth  $r, \theta$  within about 5% with DSC at 0.05147, B1 at 0.04755, and B2 at 0.05083.. Both the moderate and dense track relatively closely with each other and with the  $r, \theta$  pairs matching fairly well to ground truth. The dense set is slightly better. The results of the values for  $R_{CA}$ , and  $|R_{CA}-I|$  are given below in Table VII.

The results for  $R_{CA}$  are shown in Fig. 19 and both  $R_{CA}$

TABLE VII: RATIO CALIBRATED TO ACTUAL( $R_{CA}$ ) COMPARISON

$R_{CA}$	sparse	moderate	dense
DSC	1.1278	0.9783	0.97086
Baseline 1 (distortion)	2.0285	0.98198	0.9855
Baseline 2 (single viewpoint spherical)	1.1142	0.976033	0.9762
Baseline 3 (generic)	2.7058	1.05831	Failed

$ R_{CA}-I $	sparse	moderate	dense
DSC	0.089742	0.05147	0.0541
Baseline 1 (distortion)	1,0285	0.047553	0.0532
Baseline 2 (single viewpoint spherical)	0.1465	0.05083	0.0535
Baseline 3 (generic)	1.7058	0.19132	Failed

and  $|R_{CA} - I|$  are summarized in Table VII, which shows that the  $R_{CA}$  has the most variance for the sparse and dense cases, and the moderate is closest to actual for all four

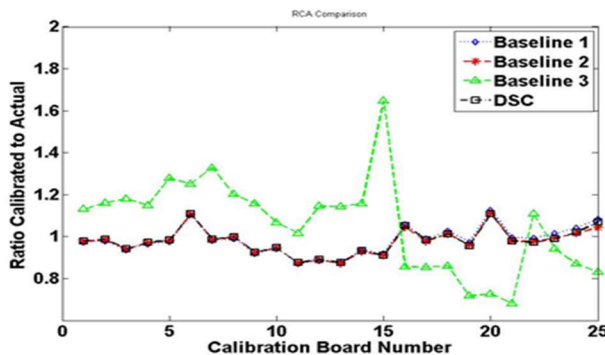


Fig. 19: Comparison ratio of calibrated to actual ( $R_{CA}$ ) for DSC method compared to the three Baseline methodologies for the moderate data set.

methods.

The results for the three comparison methods error are given in Fig. 20. The best error result is the sparse data set at 10 images with  $1.526 \times 10^{-5}$  the dense at 0.00265, and the moderate at 0.0628-pixel error.

Both the moderate and dense are due to outliers with the

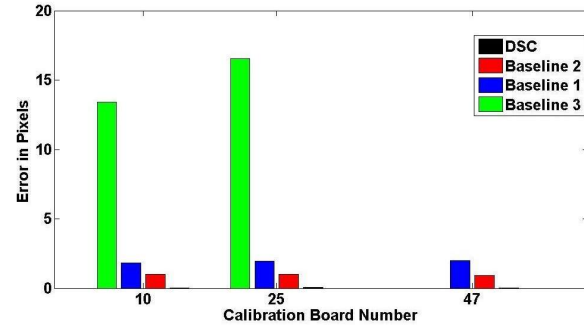


Fig.20. A comparison plot of the error for the three data sets; sparse, moderate, and dense with 10, 25, and 47 images respectively. The plot compares the average error of the four methods with DSC being near zero, Baseline 1 (distortion) and 2 (single viewpoint spherical) on the order of one to two pixels. Baseline 3 (generic) between 14 and 16 pixels for sparse and moderate datasets However, the Baseline 3 method did not work for the Dense data set and did not converge.

bulk of the data being comparable to the sparse case. The difference between 25 and 47 is so small that it isn't significant. Also, the larger number of calibration boards allows for room to throw out the outliers. This result shows that 10 images are adequate from an error standpoint. The benefit of 25 or 47 images is that if there are any problem images they can be deactivated and not used in the calibration.

The maximum error of Baseline 1 (distortion) and 2 (single viewpoint spherical) is on the order of one to two pixels, the Baseline 3 is about 16 pixels, while the DSC method is sub-pixel and near zero. Of the three methods the DSC has the lowest error less than 0.01, followed by Baseline 2 (single viewpoint spherical) at about 1 pixel and Baseline 1 (distortion) at 1.5 to 2 pixels of error, and finally Baseline 3 (generic) at 16.566 pixels of error. The added complexity of Baseline 1 and Baseline 2 are not required as the simpler DSC method gets better accuracy and comparable calibration results.

Table VI in Section V.C. shows the comparison of error, standard deviation, computation time, center, and focal length for the four methodologies. Again DSC method has the lowest computation time at under 0.032 seconds for the sparse case, 0.084 for moderate case and 0.17 for the dense case. The DSC computation time is then followed by the Baseline 1 (distortion) methodology at about 2 seconds. The Baseline 2 (single viewpoint spherical) methodology had a computation time at 12 to 54 seconds. Finally, the Baseline 3 (generic) computation time was 933 seconds.

Table VII shows the average  $R_{CA}$  for all four methods and data sets. Baseline 2 had the most consistency between data sets. The differences in  $R_{CA}$  were not sufficient to influence the final  $f(R_{CA}, \epsilon_{th}, t)$  result.

Fig. 21 shows the plot of the Pareto Optimization for the fitness function (12) for the four methods and the three data sets. The plot results are summarized in Table VIII and it can be seen from the plot that the DSC method has the best results for the fitness function followed by Baseline 1, and 2 with Baseline 3 being the least fit. Table VIII results show that  $f(R_{CA}, \epsilon, t)$  was lowest for the DSC moderate

TABLE VIII: OPTIMALITY COMPARISON

$f(R_{CA}, \epsilon, time)$	sparse	moderate	dense
DSC	0.11796	<b>0.0499</b>	0.05326
Baseline 1 (distortion)	4.0827	2.6580	21.4600
Baseline 2 (single viewpoint spherical)	1,969	6.4555	52.7600
Baseline 3 (generic)	18.130	94.70	Failed

data set. Under this image set, the Pareto-optimization provided a better RCA match, but the sparse case had the lowest error. This resulted in the overall lowest value for  $f(R_{CA}, \epsilon, t)$ . Thus the moderate data set is optimum for calibration in this case.

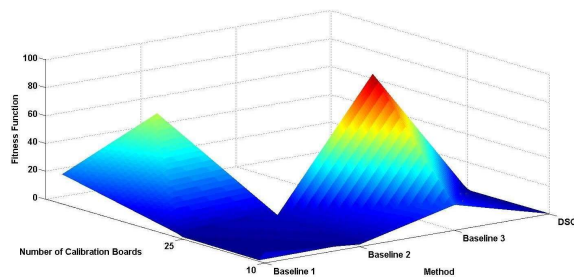


Fig. 21: Plot of the Pareto Optimization results for the fitness function from Section III.C equation (12) for the four methodologies and three data sets.

#### IV. CONCLUSION

We developed a Direct Spherical Calibration (DSC) methodology which used the four corners of the calibration board to find the center of the calibration board, and then used the direct spherical coordinates of the center of the calibration board as the re-projection points matrix was used to iteratively find the calibration parameters. Of the four methods evaluated, the DSC method had the least time, a simpler corner extraction methodology, more reliable calibration board coordinate capture, and sub pixel accuracy compared to the other three Baseline methodologies. Due to the robustness and the simplification of the DSC, it was demonstrated that it is not necessary to use the more complex methods. We did not investigate the scaling of this approach to other sensors, but it should be theoretically possible.

When using the DSC methodology, it was found that the lowest error could be found with the sparse data set. Both the moderate and dense data sets had outliers caused by the occlusion of some of the grid points and poor IR edge quality. The advantage of the larger data sets would be the

ability to throw out outliers and possibly achieve better performance as shown in the Pareto optimization analysis. However, the DSC with moderate data set had the overall optimum performance.

The elimination of outliers was not explored in this research. The results from this calibration implementation will be applied in our follow on research utilizing the omnidirectional IR and visual cameras. This calibration approach is required as a foundation for our further research into the application of these sensors for the measurement of scene material visual properties through the fusion of the O-D IR and visual streams, and ultimately to the use of a convolution neural network deep learning approach to a semantic scene reconstruction model.

#### REFERENCES

- [1] H. Anderson, A. Treptow, and T. Duckett, "Self-Localization in Non-Stationary Environments Using Omnidirectional Vision", *Robotics and Autonomous Sys.* Vol. 55, pp 541 – 551, 2007.
- [2] C. Cauchois, E. Brassart, C. Drocourt, and P. Vasseur, "Calibration of the Omnidirectional Vision Sensor: SYCLOP", in *Proc. IEEE Intl. Conf. on Robotics and Automation*, Vol. 2, pp 1287 – 1292, 1999.
- [3] S. Baker, and S. Nayar, "A Theory of Single-Viewpoint Catadioptric Image Formation", *Intl. J. of Computer Vision*, 35(2), pp 1 – 22, 1999.
- [4] G. Caron, E. Mouaddib, and E. Marchand, "3D Model based tracking for omnidirectional vision: A new spherical approach", *Robotics and Autonomous Sys.* Vol. 60, pp 1056-1068, 2012.
- [5] C. Geyer and K. Daniilidis, "Catadioptric projective geometry", *Intl. J. Computer Vision*, 43, pp 223-243, 2001.
- [6] L. Puig, J. Bermudez, P. Sturm, and J. Guerrero, "Calibration of omnidirectional cameras in practice: A comparison of methods", *Computer Vision and Image Understanding*, Vol. 116, No. 1, pp 120-147, 2012.
- [7] D. Scaramuzza, A. Martinelli, and R. Siegwart, "A Flexible Technique for Accurate Omnidirectional Camera Calibration and Structure from Motion", in *Proc. IEEE Intl. Conf. of Vision Systems (ICVS'06)*, New York, 2006.
- [8] D. Scaramuzza, A. Martinelli, and R. Siegwart, "A Toolbox for Easy Calibrating Omnidirectional Cameras", in *Proc. IEEE Intl. Conf. Intelligent Robots and Sys. (IROS 2006)*, Beijing China, 2006.
- [9] C. Mei., and P. Rives, "Single View Point Omnidirectional Camera Calibration from Planar Grids", *Proc. IEEE Intl. Conf. Robotics and Automation*, 2007.
- [10] H. Tang, Y. Liu, "Automatic Simultaneous Extrinsic-Odometry Calibration for Camera-Odometry System", *IEEE Sensors J.*, vol. 18, no. 1, pp. 348 - 355, 2018.
- [11] L. Puig, Y. Bastanlar, P. Sturm, J. Guerrero, and J. Barreto, "Calibration of Central Catadioptric Cameras Using a DLT-Like Approach", *Intl. J. Computer Vision*, 93: pp. 101–114, 2011.
- [12] Y. Motai and A. Kosaka, "Hand-Eye Calibration Applied to Viewpoint Selection for Robotic Vision", *IEEE Trans. Industrial Electronics*, Vol. 55, Issue 10, pp.3731-3741, 2008.
- [13] Y. Motai and A. Kosaka, "SmartView: Hand-Eye Robotic Calibration for Active Viewpoint Generation and Object Grasping", *Proc. IEEE Intl. Conf. Robotics and Automation*, Vol. 3, pp.2183-2190, 2001.
- [14] X. Peng, M. Bennamoun, Q. Wang, Q. Ma, and Z. Xu, "A Low-Cost Implementation of a 360° Vision Distributed Aperture System", *IEEE Trans. Circuits and Systems for Video Technology*, vol. 25, no. 2, pp. 225-238, 2015.
- [15] E. Benli, J. Ralph, Y. Motai, "Dynamic 3-D Reconstruction of Human Targets via an Omni-Directional Thermal Sensor", *IEEE Sensors J.*, vol., 18 no. 17, pp. 7209-7221, 2018.
- [16] D. Strelow, J. Mishler, D. Koes, and S. Singh, "Precise Omnidirectional Camera Calibration", in *Proc. IEEE Conf. Computer Vision and Pattern Recognition*, pp. 689-694,

December, 2001.

[17] Z. Yan, L. Zhao, and H. Wanbao, "A Survey of Catadioptric Omnidirectional Camera Calibration", *Intl. J. Information Technology and Computer Science*, Vol.5 (3), pp 13-20, 2013.

[18] H. Duan, and W. Yihong, "A Calibration Method for Paracatadioptric Camera from Sphere", *Pattern Recognition Letters*, Vol.33 (6), pp 677-684, 2012.

[19] C. Geyer, and K. Daniilidis, "Paracatadioptric camera calibration", *IEEE Trans. Pattern Analysis and Machine Intelligence*, Vol.24(5), pp 687-695, 2002.

[20] D. Santana-Cedr s, L. Gomez, M. Alem n-Flores, A. Salgado, J. Esclarin L. Mazorra, L. Alvarez, "Estimation of the Lens Distortion Model by Minimizing a Line Reprojection Error", *IEEE Sensors J.*, vol. 17, no. 9, pp. 2848 - 2855, 2017.

[21] Z. Zhang, T. Tan, K. Huang, and Y. Wang, "Practical Camera Calibration from Moving Objects for Traffic Scene Surveillance", *IEEE Trans. Circuits and Systems for Video Technology*, vol. 23, no. 3, pp. 518-533, 2013.

[22] R. Summan, G. Dobie, G. West, S. Marshall, C. MacLeod, and S. G. Pierce, "The Influence of the Spatial Distribution of 2-D Features on Pose Estimation for a Visual Pipe Mapping Sensor", *IEEE Sensors J.*, vol. 17, no. 19, pp. 6313-6321, 2018.

[23] X. Ying and Z. Hu, "Catadioptric camera calibration using geometric invariants", *IEEE Trans. Pattern Analysis and Machine Intelligence*, Vol. 26, Issue 10, pp. 1260 - 1271, 2004.

[24] X. Deng, F. Wu, Y. Wu, F. Duan, L. Chang, and H. Wang, "Self-calibration of hybrid central catadioptric and perspective cameras", *Computer Vision and Image Understanding*, Vol.116 (6), pp. 715-729 2012.

[25] S. Ramalingam, P. Sturm and S. Lodha "Generic Self Calibration of Central Cameras", *Computer Vision and Image Understanding*, Vol.114, pp. 210-219, 2010.

[26] L. Kr ger, and C. W hler, "Accurate chequer board corner localization for camera calibration", *Pattern Recognition Letters*, Vol.32 (10), pp.1428-1435, 2011.

[27] J. Barreto, and H. Araujo "Geometric properties of central catadioptric line images and their application in calibration", *IEEE Trans. Pattern Analysis and Machine Intelligence*, Vol.27 (8), pp.1327-33, 2005.

[28] J. Barreto "A unifying geometric representation for central projection systems", *Computer Vision and Image Understanding*, Vol.103 (3), pp.208-217, 2006.

[29] A. Bonarini, P. Aliverti, and M. Lucioni. "An Omnidirectional Vision Sensor for Fast Tracking for Mobile Robots", *IEEE Trans Intelligent Transportation Systems*, VOL. 49(3), 2000.

[30] A. Agrawal, S. Ramalingam. "Single image calibration of multi-axial imaging systems." *Proc. Computer Vision and Pattern Recognition (CVPR)*, pp 1399-1406, 2013.

[31] L. Zhou, "A New Minimal Solution for the Extrinsic Calibration of a 2d LIDAR and a Camera Using Three Plane-Line Correspondences", *IEEE Sensors Journal* Vol. 14, no. 2, pp. 442-454, 2014.

[32] J. Y. Bouguet. (2013, Oct. 10). *Camera Calibration Toolbox* Available: [http://www.vision.caltech.edu/bouguetj/calib\\_doc](http://www.vision.caltech.edu/bouguetj/calib_doc)

[33] J. Kannala, J. Heikkil  and S. Brandt. "Geometric camera calibration". Wiley Encyclopedia of Computer Science and Engineering, 2008.

[34] J. Kannala and S. Brandt. "A generic camera model and calibration method for conventional, wide-angle and fish-eye lenses". *IEEE Trans. Pattern Analysis and Machine Intelligence*, vol. 28, no. 8, 2006.

[35] W. Wong, C. Loo and W. Lim, "Optical Approach Based Omnidirectional Thermal Visualization", *Intl. J. Image Processing*, Vol. 4(3). pp. 263, 2010.

[36] O. Romain, T. Ea., and P. Garda, "Multispectral omnidirectional vision sensor: design, calibration, and utilization", *Optical Engineering*, Vol.46 (10), 12 pages, 2007.

[37] T. Mouats, N. Aouf, L. Chermak, and M. A. Richardson, "Thermal stereo odometry for UAVs," *IEEE Sensors J.*, vol. 15, no. 11, pp. 6335-6347, Nov. 2015.

[38] S. You, R. Wei, A. Robles-Kelly, "A Multiview Light Field Camera

for Scene Depth Estimation from a Single Lens", *Proc. AML arXiv*, 2016.

[39] S. You, R. Tan, R. Kawakami, Y. Mukaigawa and K. Ikeuchi, "Water drop Stereo", in *Computing Research Repository arXiv*, vol. 1604.00730, 2016.

[40] G. Agrawal, K. Lewis, K. Chung, C-H. Huang S. Parashar, and C. Bloebaum, "Intuitive Visualization of Pareto Frontier for Multi-Objective Optimization in n-Dimensional Performance Space", *American Institute of Aeronautics and Astronautics, Technical Report*, 2004.

[41] E. Zitler M. Laumans, and S. Bleuler, "A Tutorial on Evolutionary Multiobjective Optimization", *Springer, Metaheuristics for Multiobjective Optimization, Lecture Notes Economics and Mathematical Systems*, Vol.535, pp. 3-37, 2004.



**David Stone** (M'10) received the B.S Eng. Degree in electrical and electronic engineering from Purdue University, West Lafayette, IN, USA in 1973, the M.S. Eng. Degree in Mechanical Eng. and Ocean Engineer Degree from Massachusetts Institute of Technology, Cambridge, MA, USA in 1982. He currently works full time for the Naval Surface Warfare Center Dahlgren, Dahlgren, VA. His research interests include deep neural networks and intelligent robotic perception.



**Guarav Shaw** (M'13) received the B. commerce, economics, and accounting from The Maharaja Sayajirao University of Baroda in 2005, the BS. Computer Eng. In biophysics from Virginia Commonwealth University, Richmond, VA, USA in 2014. He is currently a web integration developer at Bon Secours Health Systems, Richmond, VA, USA. His research interests include web, mobile and data integration in health care, and backend and database programming.



**Yuichi Motai** (S'00-M'03-SM'12) received the B.Eng. degree in instrumentation engineering from Keio University, Tokyo, Japan, in 1991, the M.Eng. degree in applied systems science from Kyoto University, Kyoto, Japan, in 1993, and the Ph.D. degree in electrical and computer engineering from Purdue University, West Lafayette, IN, U.S.A., in 2002. He is currently an Associate Professor of Electrical and Computer Engineering at Virginia Commonwealth University, Richmond, VA, U.S.A.

His research interests include the broad area of sensory intelligence; particularly in medical imaging, pattern recognition, computer vision, and sensory-based robotics.